Scientific paper

Tension stiffening of reinforced concrete affected by radiation-induced volume expansion of aggregate

Daisuke Kambayashi[1], Ippei Maruyama[2*,3], Osamu Kontani[4], Shohei Sawada[5], Takahiro Ohkubo [6], Kenta Murakami [7], Kiyoteru Suzuki [8]

[1] Engineer, Nuclear Power Department, Kajima Corporation, Tokyo, Japan. (former graduate student at Nagoya University)
kambayad@kajima.com
[2] Professor, Graduate School of Engineering, The University of Tokyo, Tokyo, Japan.
[*]Corresponding author, *E-mail:* i.maruyama@bme.arch.t.u-tokyo.ac.jp

[3] Professor, Graduate School of Environmental Studies, Nagoya University, Nagoya, Japan.
[4] Principle Engineer, Nuclear Power Department, Kajima Corporation, Tokyo, Japan.
[5] Group Leader, Nuclear Power Department, Kajima Corporation, Tokyo, Japan.
[6] Assoc. Prof., Graduate School of Engineering, Chiba University, Chiba, Japan.
[7] Assoc. Prof., Graduate School of Engineering, The University of Tokyo, Toyo, Japan.
[8] Research director, Societal Safety and Industrial Innovation Division, Mitsubishi Research Institute, Inc., Tokyo, Japan.

Abstract

The tension stiffening behaviors of reinforced concrete (RC) prisms affected by aggregate volume expansion induced by neutron irradiation were numerically investigated using a rigid body spring network model. First, the model was validated by comparison with the uniaxial tension test results of wet- and dry-cured (with volume contraction of concrete) RC prisms. Then, different degrees of expansion strain were applied to the aggregate elements in the RC prism model and uniaxial tension loading was again simulated. Tension stiffening decreased under larger radiation-induced volume expansion of the aggregate owing to the corresponding decrease in the concrete tensile strength with increasing damage, this behavior changed dramatically according to restraint condition. Indeed, the Young's modulus of restrained concrete after aggregate expansion was larger than that of unrestrained concrete after aggregate expansion. However, the compressive stress in the concrete after aggregate expansion was effectively transmitted to the rebar during uniaxial tension loading; this behavior indicated even after 0.5% aggregate expansion, RC can maintain its integrity under uniaxial tension.

Keywords: Tension stiffening, Radiation-induced volume expansion, Aggregate, Bond

1. Introduction

Nuclear power plants represent an essential basic source of electrical power. Therefore, ensuring the long-term operation of nuclear power plants is a critical social issue that must be addressed. From a concrete engineering perspective, there is a lack of data and experience for evaluating the integrity of concrete members exposed to neutron and gamma irradiation environments. The deterioration of concrete owing to neutron exposure is caused by radiation-induced volume expansion (RIVE) of the aggregate (Elleuch et al., 1972; Hilsdorf et al., 1978; Maruyama et al., 2017). The most neutron-sensitive rock-forming mineral found in aggregate is α-quartz (Wittels and Sherrill, 1954; Primak, 1958; Denisov et al., 2012; Field et al., 2015; Maruyama et al., 2017; Le Pape et al., 2018, 2020). As the hollow cylindrical biological concrete shield (BCS) wall of a nuclear power plant is particularly affected by neutron exposure, ensuring its seismic, support, and shielding performance over time is an essential consideration; several evaluations have accordingly been conducted for this purpose (Le Pape, 2015; Bruck et al., 2019; Kambayashi et al., 2020). The results have indicated that a) the ring tension in the outer part of a BCS subjected to RIVE leads to the development of radial cracks, b) the temperature distribution owing to gamma heating also increases the risk of radial cracks, and c) circumferential cracks occur in the concrete near the internal surface of the BCS owing to neutron attenuation and the resultant different degrees of RIVE distributed along the radial direction. In particular, the tension stiffening performance of reinforced concrete can deteriorate if the aggregate near the reinforcing bars (rebars) develops RIVE, as the resultant cracks and their opening widths may affect the bond between the concrete and rebar. This can reduce the seismic performance of the entire BCS structure. To investigate this concern, a fundamental numerical study was conducted to determine how RIVE of aggregate affects the tension stiffening performance of reinforced concrete.

2. Numerical calculation

2.1 Rigid body spring network model

This study employed the rigid body spring network model (RBSM) originally developed by Kawai (1978). In RBSM modeling, rigid bodies are connected by springs described using a set of nonlinear constitutive laws to model the fracture behavior of the analyzed object. The interface between each body is divided into several triangles drawn from the barycenter of the interface, each attached to three individual springs: one to transmit the normal force and two to transmit the orthogonal shear forces, as shown in Fig. 1 (Yamamoto et al., 2008). The bending moment across the contact surface (indicated by the gray-colored pentagon in Fig. 1) is expressed by the springs provided at the center of gravity of each triangle subdivision. Nonlinear behavior can be evaluated by considering the softening of the springs in the normal and shear directions.

Because RBSM uses discontinuous elements, complex behaviors such as cracking can be easily reproduced. However, because the element boundary surfaces are also regarded as the crack surfaces, the crack generation and development are significantly affected by the size and arrangement of the elements. This study employed a random element geometry based on Voronoi diagrams (Bolander and Saito, 1998).

The concrete components considered in the model were the coarse aggregate and mortar; in addition, rebar elements and the interfacial transition zone (ITZ) between the aggregate and mortar were also included.

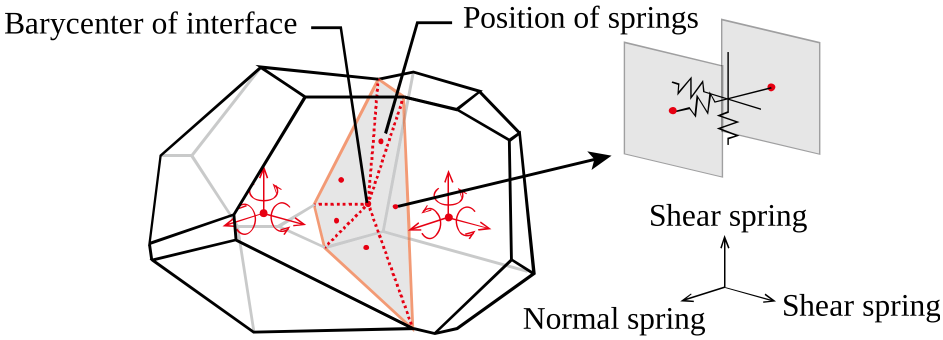

Fig. 1 Schematic of the elements in the RBSM and the location of springs connecting them.

2.2 Constitutive laws for the mortar, aggregate, and steel springs

Based on previous studies, constitutive laws for aggregate, mortar, and steel springs (Yamamoto et al., 2008, 2014; Sasano et al., 2020; Sasano and Maruyama, 2021) were introduced as given in the schematics and equations in Fig. 2, where σ^* is the stress in a normal spring; ε^* is the strain in a normal spring; ε_t^* is the strain at the tensile strength of a normal spring; f_c^* is the compressive strength of a normal spring; f_t^* is the tensile strength of a normal spring; E_c^* is the Young's modulus of a normal spring; G_{ft}^* is the fracture energy of a normal spring; h^* is the length between adjacent elements (mm); τ^* is the stress in a shear spring; γ^* is the strain in a shear spring; τ_f^* is the shear strength of a shear spring; γ_f^* is the strain at the shear strength of a shear spring; φ^* is the internal friction angle of a shear spring; K^* is the softening slope of a shear spring; β_{cr}^* is the shear reduction factor; c^* is the cohesion of a shear spring; β_0^*, β_{max}^*, and χ^* are constants for the shear softening slope; σ_b^* is a constant used to determine the limit of the shear strength increase; and κ^* is a constant used to determine β_{cr}^* and E_c^*. In the constitutive laws, compression failure is not explicitly considered, as shown in Fig. 2(c), and the failure of brittle materials under compression load is reproduced by compression shear failure.

In this study, the spring parameters were calculated by multiplying the experimentally obtained concrete properties by a factor, as shown in **Tables 1** and **2**. In the target experiment (Shima et al., 1987), only the compressive strength was investigated; the remaining parameters were determined using experimental results (Maruyama et al., 2014). The fracture energy of the mortar was calculated using the following equation (JSCE 2002):

$$G_{ft} = 10 \cdot (d_{max})^{1/3} \cdot f_c^{\,1/3}, \tag{1}$$

where G_{ft} is the fracture energy (N/mm^2), d_{max} is the maximum aggregate diameter (mm), and f_c is the compressive strength (N/mm^2). The fracture energy of the aggregate was based on the results of a previous study (Friedman et al., 1972), and that of the ITZ was considered to be the average of the fracture energies of the aggregate and mortar.

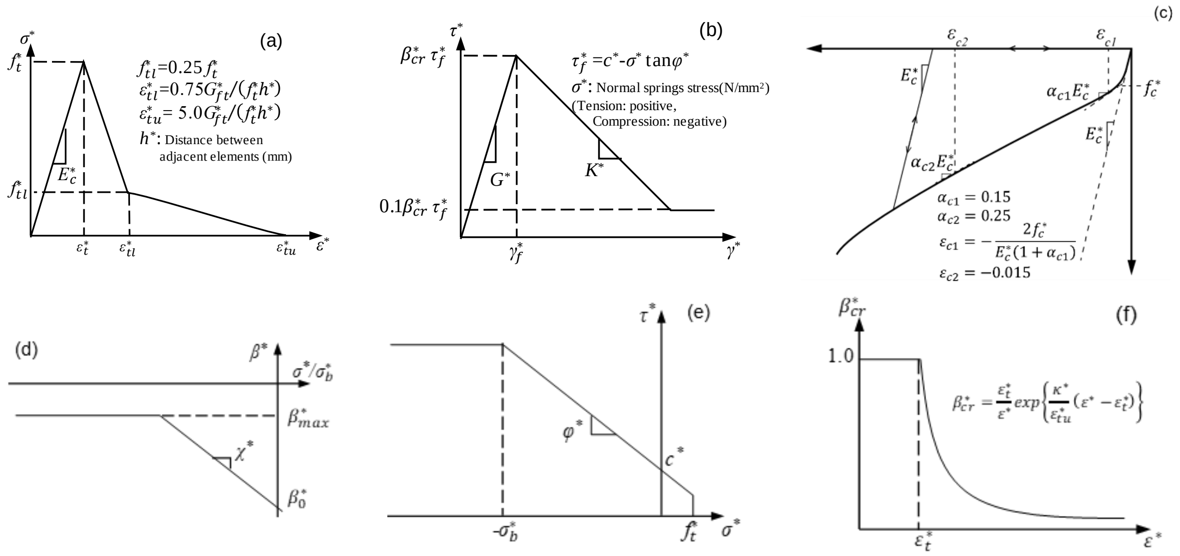

Fig. 2 Constitutive laws for mortar and aggregate: (a) tensile model for the normal spring, (b) shear spring model, (c) compression model for the normal spring, (d) softening coefficient of the shear spring, (e) Mohr–Coulomb criteria for the shear spring, and (f) shear reduction coefficient. In this figure, E_c^* denotes E_{cm}^* for mortar, E_{ca}^* for aggregate, and E_{cc}^* for concrete; the same notation is applied for f_t^*, G_{ft}^*, G^*, and c^*.
Figures after (Yamamoto et al., 2008, 2014; Sasano et al., 2020; Sasano and Maruyama, 2021)

Table 1 Relationships between spring parameters for the normal springs describing mortar, aggregate, and steel elements and their macroscopic material properties (shown in Table 3).

	E_c^* (N/mm²)	f_t^* (N/mm²)	G_{ft}^* (N/m)
Mortar	$1.45E_{cm}$	$0.8f_{tm}$	$0.5G_{ftm}$
Aggregate	$1.45E_{ca}$	$0.8f_{ta}$	$0.5G_{fta}$
Steel	$1.00\ E_s$	$1.0\ f_{ts}$	-

Note c: compressive, t: tensile, ft: tensile fracture, m: mortar, a: aggregate, s: steel.

Table 2 Factors describing the relationships between the shear spring parameters for the mortar, aggregate, and steel elements and the corresponding macroscopic material properties.

	$\eta_c^* = G^*/E^*$	c^* (MPa)	φ^* (degree)	σ_b^* (MPa)	β_0^*	$\beta_{\max}^*$	χ^*	κ^*
Mortar	0.35	$0.14\ f_{cm}$	37	$0.55\ f_{cm}$	-0.05	-0.025	-0.01	-0.3
Aggregate		$0.14\ f_{ca}$		$0.55\ f_{ca}$				
Steel	0.38	-	-	$0.55\ f_{cs}$				

Table 3 Physical properties of the material components used in the constitutive calculations.

	E (MPa)	f_t (MPa)	f_c (MPa)	G_{ft} (N/m)
Mortar	16,900	3.79	46.6	0.0615
Aggregate	70,000	3.79	150.0	0.0615
Steel	205,000	625.0	625.0	-

2.3 Constitutive laws for the ITZ (Kambayashi et al., 2020)

Fig. 3 shows the constitutive laws for the ITZ between the mortar and aggregate, where the coefficients α_{ITZ}, β_{ITZ}, γ_{ITZ}, and η_{ITZ} were all set to 0.5 in this study. The ITZ has a lower strength and Young's modulus than the mortar; these are significant properties for evaluating the cracking behavior of concrete. The Young's modulus and strength in the tensile region of the ITZ were set equal to half the mortar values in this study, and the constitutive law for the shear springs was the same as that of the mortar. The modulus and strength in the compressive region were defined as the averages of those for the aggregate and mortar. Because information concerning the ITZ is scarce, its fracture energy was assumed to be equal to half that of the mortar. For the physical properties of the ITZ between the mortar and other elements, the values were weighted according to the corresponding spring lengths; the same rules were applied for the ITZ between the mortar and steel as for the ITZ between the mortar and aggregate.

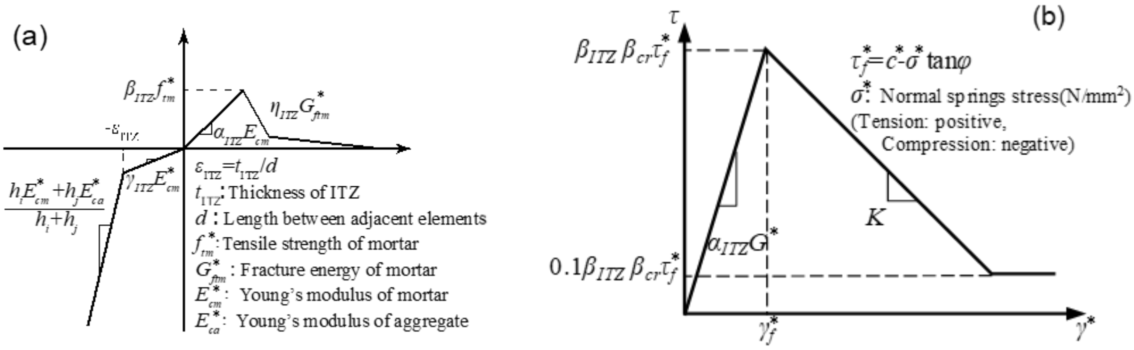

Fig. 3 Constitutive laws for the mortar–aggregate ITZ in (a) tension and compression and (b) shear.

2.4 Impact of drying shrinkage

Simulations of wet-cured (Specimen 1) and dry-cured (Specimen 2) concrete were evaluated against the results of a reference experiment to verify the performance of the RBSM. In the dry-cured specimen, moisture transport was considered using a truss network model (Bolander and Berton, 2004). The moisture transport parameters were determined based on previously obtained mass-loss data (Maruyama et al., 2014) to comprise a diffusion coefficient of 300 mm^2/day and a moisture transfer coefficient at the boundary of 15.8 mm/day. To consider the change in the physical properties of the mortar during drying, the spring parameters describing the Young's modulus and strength were adjusted according to the change in relative water content ΔR, as shown in Fig. 4; this approach has been validated elsewhere (Sasano and Maruyama, 2021). Furthermore, mortar shrinkage was considered based on its relationship with ΔR, as shown in Fig. 5 (Sasano et al., 2020). According to the slope of the curve in the figure, the final ΔR was set to 0.45 in the present calculation. A linear relationship between ΔR and shrinkage was assumed for the aggregate elements; the shrinkage at a ΔR of 0.45 was assumed to be –50 με.

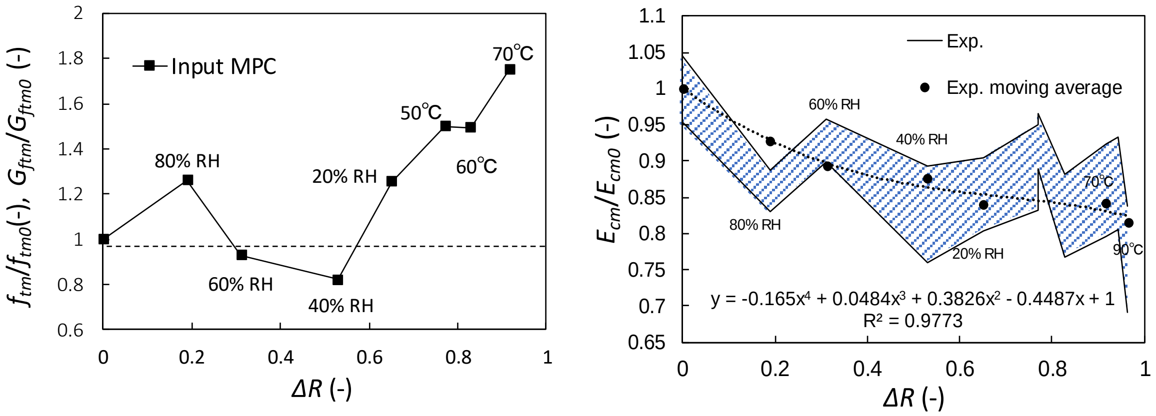

(a) (b)

Fig. 4 Spring parameter values as a function of relative water content change (ΔR): (a) mechanical property change (MPC) ratio of the mortar for tensile strength or fracture energy and (b) Young's modulus of the mortar. (Sasano et al., 2020)

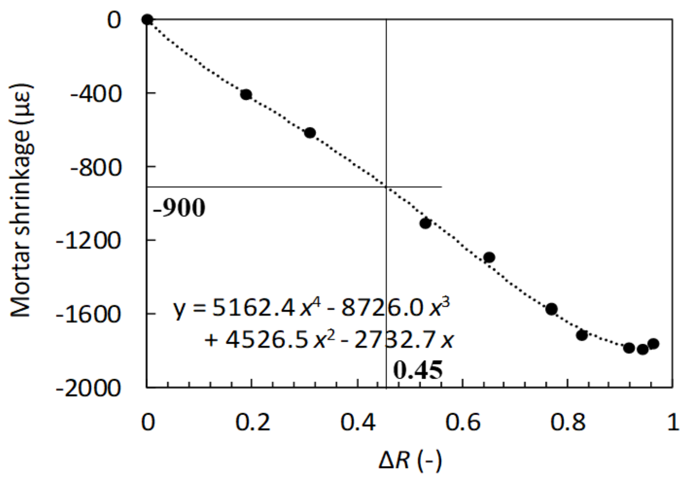

Fig. 5 Relationship between relative water content change (ΔR) and shrinkage of the mortar elements.

2.5 Reference experiment (Shima et al., 1987)

The reference experiments used for comparison in this study were undertaken by Sima et al. (1987), who conducted a substantial experimental campaign to understand bond behavior from the perspective of reinforced concrete (RC) member design. One of their experiments conducted tensile testing of rebar embedded along the center of a long rectangular concrete prism, as shown in Fig. 6.

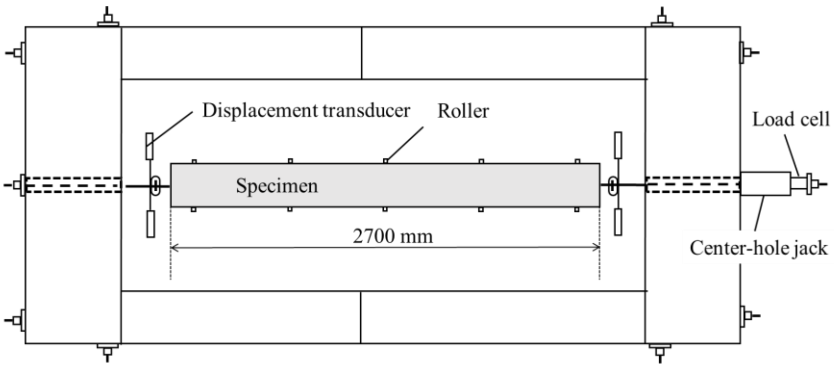

(a) Overall setup

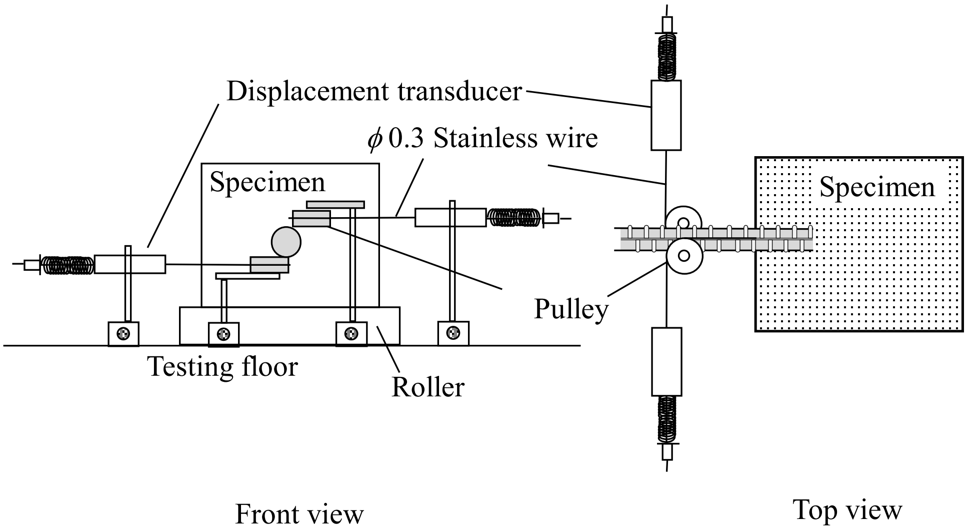

(b)

Fig. 6 Setup of RC prism loading experiment (Shima et al., 1987). (a) overall setup and (b) Sections of setup.

In this experiment, "the bar was fixed along the form with a special attention to arrange the bar straightly," and the concrete was placed in the direction perpendicular to the embedded rebar. Specimen 1 was cured in water until one day before the test to prevent drying shrinkage, while Specimen 2 was cured in air to investigate the influence of drying shrinkage. It should be noted that the strengths of specimens 1 and 2 might not be comparable owing to insufficient curing conditions; however, considering the lack of compressive strength data, the same physical properties were assumed in the calculation for the wet- and dry-cured concrete.

The size of each concrete prism was 2700 × 150 × 250 mm^3, the reinforcement ratio was 1.0%, and a single 19 mm (D19) diameter deformed bar was used. The compressive strength of the concrete was 45 MPa. As a longer specimen was necessary to determine the appropriate average tensile strain and average stress in the rebar of a cracked RC member, the specimen lengths were determined accordingly. The stress in the rebar cannot be measured directly; therefore, 1) a 5-mm strain gauge was attached to the rebar surface every ten ribs and 2) the stress–strain relationship for steel was used to convert the measured strain to stress.

A jack was used to apply tensile force to the rebar in the specimen, which was horizontally installed in a prestressed concrete frame on the floor as shown in Fig. 6(a); one end of the rebar was fixed to the frame and the other end was connected to the jack. The friction at the bottom of the specimen was controlled using rollers (Fig. 6 (b), left). Pulleys were connected by steel wires to displacement meters fixed to the floor, and the displacement and strain values for the RC prism were calculated using the average of two values measured on opposite surfaces of the rebar (Fig. 6 (b)).

2.6 Research strategy

The objective of this research was to investigate the impact of aggregate expansion owing to neutron irradiation on the tension stiffening behavior of RC and discuss it from the perspective of aging management for concrete members affected by RIVE. The RBSM spring parameters are initially calibrated using the results of standard cylindrical specimen (Fig. 7) compressive loading tests. In this study, the same RBSM was extrapolated to the RC prisms by increasing the element size. First, the calculations for specimens 1 and 2 were validated by comparison with the reference data (Shima et al., 1987).

The average strain and stress in each RC prism specimen were calculated. The average load that the rebar responds to was required to represent the tension stiffening effect of concrete. To determine this load, half the size of the specimen was applied considering symmetry, as shown in Fig. 8. The typical element size was 20 mm, corresponding to the maximum size of the aggregate. For Specimen 2, the aggregate shrinkage was set to -50 με and the shrinkage of mortar was assumed to be -900 με. The purpose of considering moisture transport was to introduce the shrinkage of elements in the appropriate order from the surface to the inside and thereby simulate the damage to the concrete prism as it dries. Because there was no curing period or drying condition specified for Specimen 2 in the original reference (Shima et al., 1987), the moisture transport potential was set by considering a relative water content change of 0.45, and the drying calculation period was assumed to be 12 months. This period is likely unrealistic for an experimental campaign, but as a drying shrinkage experiment for a 100 × 100 × 400 mm^3 specimen would require longer than 6 months, a 12 month period should appropriately capture the impact of drying. After calculating the drying and force equilibrium cycles, the tensile loading of the RC prism was simulated.

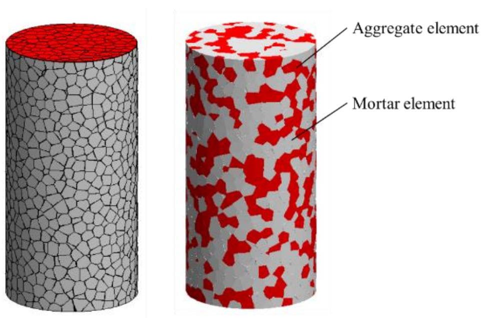

Fig. 7 RBSM mesh for a concrete cylinder; the total volume of aggregate elements is 35% of the total specimen volume.

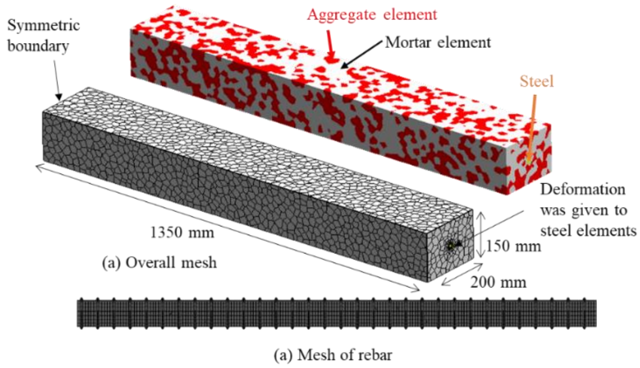

Fig. 8 RBSM mesh of RC prism.

Table 4 Input volume changes for mortar and aggregate elements.

Condition		Mortar expansion(+) /shrinkage(-)	Aggregate expansion(+) /shrinkage(-)	Corresponding neutron fluence (≧0.1 MeV @ 50 °C)
Dry-cured		-900 με	-50 με	-
Expansion	Exp-0.1	0 με	1000 με	1.9×10^{19}
	Exp-0.2		2000 με	2.5×10^{19}
	Exp-0.5		5000 με	3.4×10^{19}

These calculations were conducted to confirm the potential use of RBSM to reproduce the impact of volume change (shrinkage) of the components. The impact of RIVE on tension stiffening is then investigated by subsequently applying aggregate expansion using a similar mechanism. The volume changes applied to the elements are summarized in Table 4. It should be noted that actual accelerated irradiation experiments can only be conducted in a nuclear research reactor, and such extensive experiments cannot be conducted at a scale on which the impact of tension stiffening can be confirmed owing to the limited size of the irradiation holes in nuclear research reactors, impact of gamma-ray heating, limitations of the hot cell facility, and cost of such experiments. As a result, only numerical calculations can provide information describing the investigated issue.

Different levels of aggregate expansion were therefore employed in a series of calculations evaluating the impact of RIVE, as shown in Table 4. The considered aggregate linear expansion cases were 1000, 2000, and 5000 με; the expected corresponding neutron fluences (≧0.1 MeV at 50 °C) based on Eqs. (3) and (4) in (Maruyama et al., 2017) are shown in the far right column of Table 4. The expansion was homogenously introduced to all aggregate elements in this study, whereas in reality, the neutron dose attenuates with depth owing to the interaction between the neutrons and concrete elements. This assumption was made to facilitate the determination of the impact of RIVE on the tension stiffening behavior of concrete and avoid difficulties associated with considering the effects of cracks owing to the inhomogeneous volume expansion of the aggregate in the concrete; a more realistic case should be discussed in the future.

3. Numerical calculation results

3.1 Concrete properties

The calculated stress–strain relationships for the cylindrical concrete specimens ($\phi150\times300$ mm^3) are shown in Fig. 8. The compressive strength of the control specimen (wet-cured) was 41 MPa (in the reference experiment, it was 45 MPa) and its Young's modulus was 25 GPa (not determined in the reference). The dry-cured specimen exhibited a slightly lower concrete strength of 40 MPa, whereas its Young's modulus decreased significantly to 16 GPa; equivalent data were not reported in the reference. The drying shrinkage of the concrete was 500 με, which was not reported in the reference either.

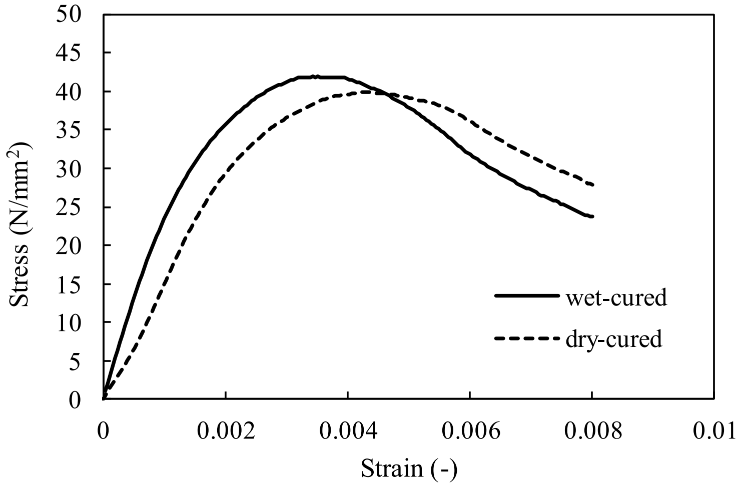

Fig. 9 Compressive stress–strain relationships for wet-cured and dry-cured concrete cylinders calculated by RBSM.

3.2 Impact of drying shrinkage

The calculation results for Specimen 1 (wet-cured) are shown in Fig. 10 and Fig. 11. Fig. 10 shows the crack distribution in the wet-cured specimen during rebar yielding. Unfortunately, asas Shima et al. (1987) did not report any cracking behavior in either specimens 1 or 2, this behavior cannot be compared. Three through cracks per 1350 mm length were observed in the results of the RBSM calculation in this study, which is relatively consistent with the five through cracks observed in the 2700 mm length of another specimen (Specimen 4 shown in Fig. 5.5 in Shima et al. (1987)), which had a reinforcement ratio of 0.6% and a compressive strength of 25 MPa after drying. Based on Japanese (AIJ) guidelines (AIJ, 2006; Nakagawa et al., 2008) the corresponding bond loss length was approximately 400 mm; therefore, the obtained crack distribution was considered reasonable. The relationship between the total load and the average strain in the wet-cured RC prism is shown in Fig. 11, where the results of the RBSM simulation are compared with the experimental data. Overall, the load–strain trend was effectively reproduced. Furthermore, the loads borne by the concrete and rebar were separated by subtracting the load in the steel elements, and the simulation results were determined to reproduce the experimental results reasonably well.

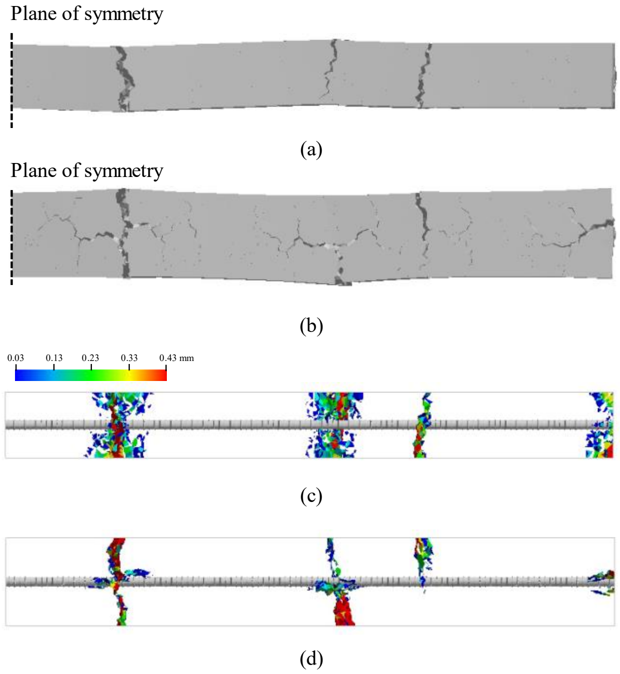

Fig. 10 Simulated cracks in Specimen 1 at the initiation of rebar yielding.
(a) Deformation of side view, (b) deformation of top view, (c) crack distribution of side view, and (d) crack distribution of top view.

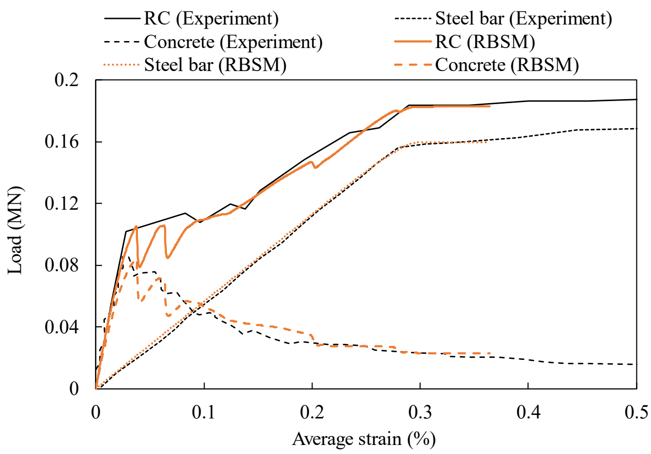

Fig. 11 Comparison of calculation results and experimental data describing the load–average strain relationships for the RC, steel rebar, and concrete of Specimen 1.

The RBSM calculation results for Specimen 2 (dry-cured) are shown in Fig. 12 and Fig. 13. Fig. 12 shows the crack distribution immediately after completion of dry curing as well as the crack distribution at rebar yield. The dry curing process increased the number of through cracks at rebar yield from three to five over the length of the specimen. The corresponding bond loss length based on the AIJ guidelines was approximately 200–300 mm; therefore, the RBSM results seem reasonable. Furthermore, the calculated relationship between the load and average strain is shown in Fig. 13 to be consistent with the experimental data. In the case of Specimen 2, the stress in the rebar at the beginning of loading should be compressive owing to the drying shrinkage of the concrete; however, as Shima et al. (1987) did not report any stress in the rebar as a result of drying shrinkage, no comparison could be made. Comparing the calculated and experimental loads at approximately an average strain of 0.05%, the RBSM calculation appears to overestimate the concrete shrinkage as the experimental load was slightly larger than that applied in the RBSM calculation. However, these results illustrate the potential of the RBSM calculation for reproducing behavioral mechanisms that can be confirmed through experiments.

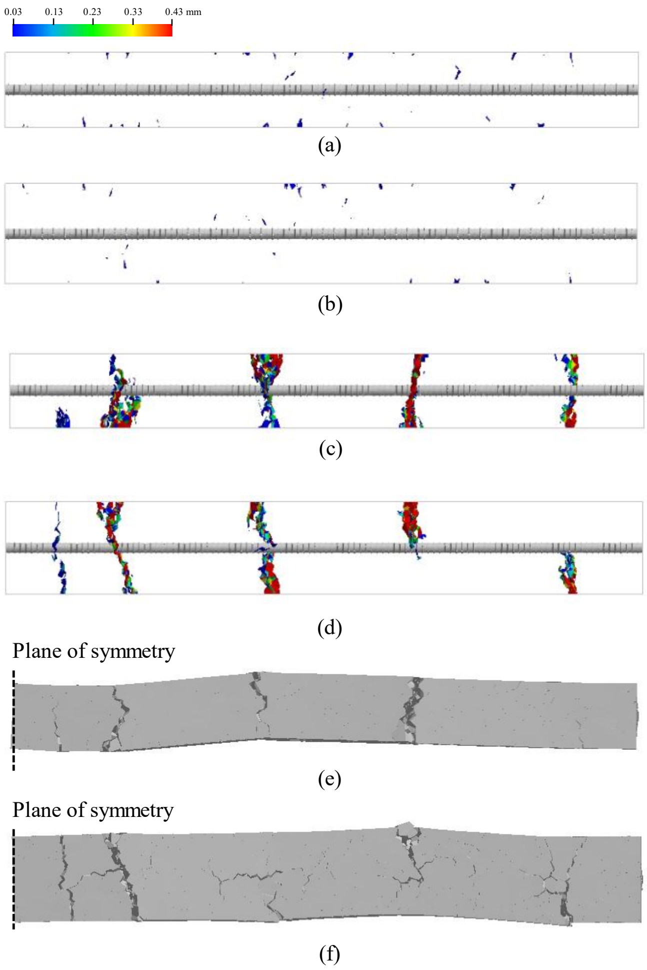

Fig. 12 Simulated cracks in Specimen 2. (a) crack distribution before loading of side view, (b) crack distribution before loading of top view, (c) crack distribution at start of rebar yielding of side view, (d) crack distribution at start of rebar yielding of top view, (e) crack distribution of side view, and (f) crack distribution of top view.

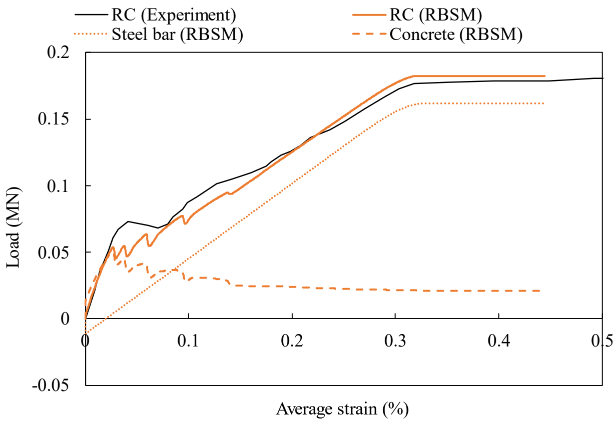

Fig. 13 Comparison of RBSM calculation results with experimental data describing the load–average strain relationships for Specimen 2.

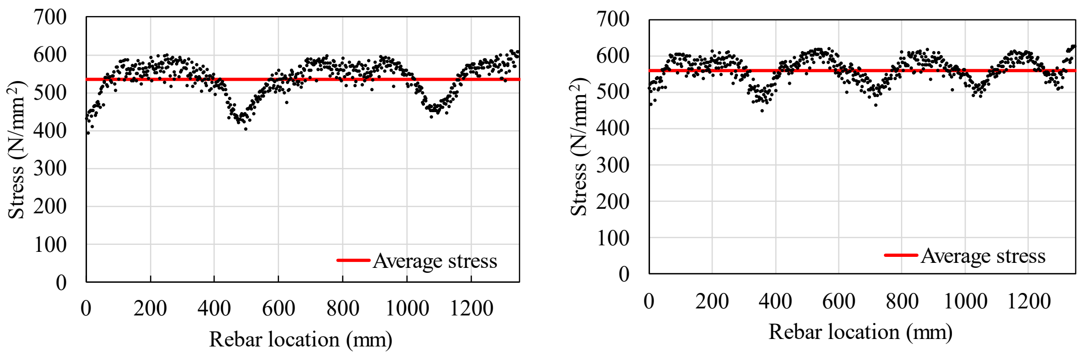

(a) (b)

Fig. 14 Comparison of rebar stress distribution in main rebar of specimens 1 (a) and 2 (b).

The stress distributions along the longitudinal axis of the rebar elements are shown in Fig. 14, which indicates that the bond loss length decreased and the minimum stress in the rebar—observed at the center of the span between cracks—increased when the concrete was dry cured. This can be explained by 1) the apparent strength reduction caused by the shrinkage-induced tensile stress in the concrete prior to loading, and 2) the reduction in the concrete tensile strength owing to damage created around the aggregate (Lin et al., 2015). Consequently, the contribution of the load borne by the rebar increased at the beginning of yielding.

3.3 Impact of RIVE of aggregate

Based on the results presented in Section 3.2, different degrees of expansion strain were applied to all aggregate elements in the RBSM mesh of the RC prism. The same loading procedure and parameters were then applied to the RC prisms as for the wet-cured specimen in Section 3.2. The crack patterns of the RC prisms immediately after the initiation of rebar yielding are summarized in Fig. 15. The stress distributions along the longitudinal axis of the rebar elements immediately after the initiation of rebar yielding are shown in Fig. 16. In addition, the load–average strain relationships of RC prisms subjected to RIVE are summarized in Fig. 17. In general, an increase in the RIVE-induced strain in the aggregate increased the number of through cracks owing to the reduction in the tensile strength of the concrete via damage around the aggregate (Sasano et al., 2020). In case of Exp-0.5, the significant pre-cracking caused by RIVE of the aggregate limited the development of discrete cracks that otherwise serve to reduce the length of the concrete–rebar bond (Fig. 15(c)); instead, homogenous crack development was observed. This behavior is confirmed by the contents of Fig. 17: in the case of Exp-0.1, a clear sudden decrease in load was observed owing to discrete crack development, whereas in the cases of Exp-0.2 and Exp-0.5, a smooth load increase was confirmed as a function of the average strain. This result suggests that discrete crack development is mitigated by the preloading cracks induced by RIVE of aggregate.

The damage to the concrete owing to RIVE is also confirmed by the change in the initial stiffnesses of the RC prisms, as shown in Fig. 17; as the expansion strain in the aggregate increased, the stiffness of the RC prisms decreased. When the expansion strain was applied to the aggregate, the compressive stress of the concrete was engaged as a consequence of self-balancing forces in the RC prism; tensile stress developed in the rebar to counteract this compressive force. Therefore, the average strain range in the RC prism during the tensile loading test increased as the RIVE-induced compression stress postponed fracture in the concrete. Theoretically, it is possible that tensile stress peak of concrete occurs after yielding of rebar.

In the case of a bare rebar, yielding will begin at a strain of ~0.3%, which is comparable with the result for Specimen 1 (0.28%), as shown in Fig. 17. However, the average strain at rebar yield decreased with increasing expansion strain owing to the accumulation of tensile stress in the rebar prior to loading as a result of RIVE. In the case of Exp-0.5, the average strain was approximately 0.13% when the rebar began to yield. The difference between the strains in Specimen 1 and Exp-0.5 was 0.17%, which is a consequence of stress accumulation in the concrete and rebar owing to RIVE of the aggregate.

Interestingly, the average strain of 0.13% observed in the rebar of Exp-0.5 when it began to yield is significantly smaller than the applied aggregate expansion strain of 0.5%. This suggests that the concrete remained in compression in some parts of the RC prism.

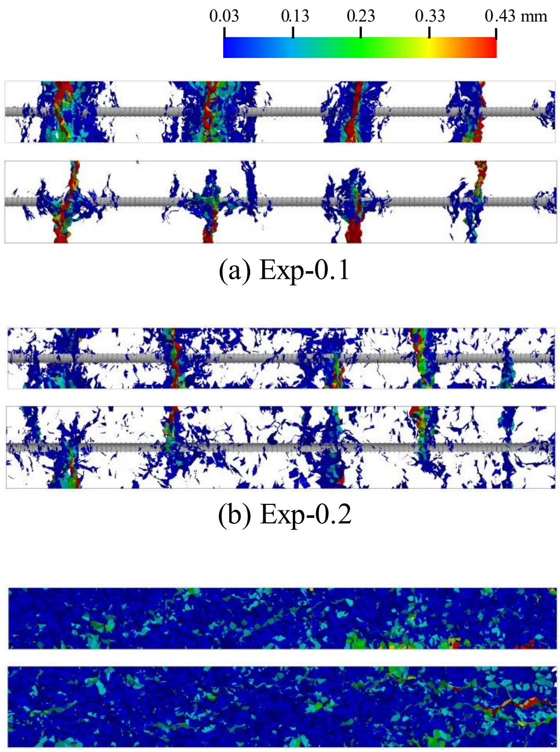

(a) Exp-0.1

(b) Exp-0.2

(c) Exp-0.5

Fig. 15 Cracks in RC prisms immediately following the initiation of rebar yielding

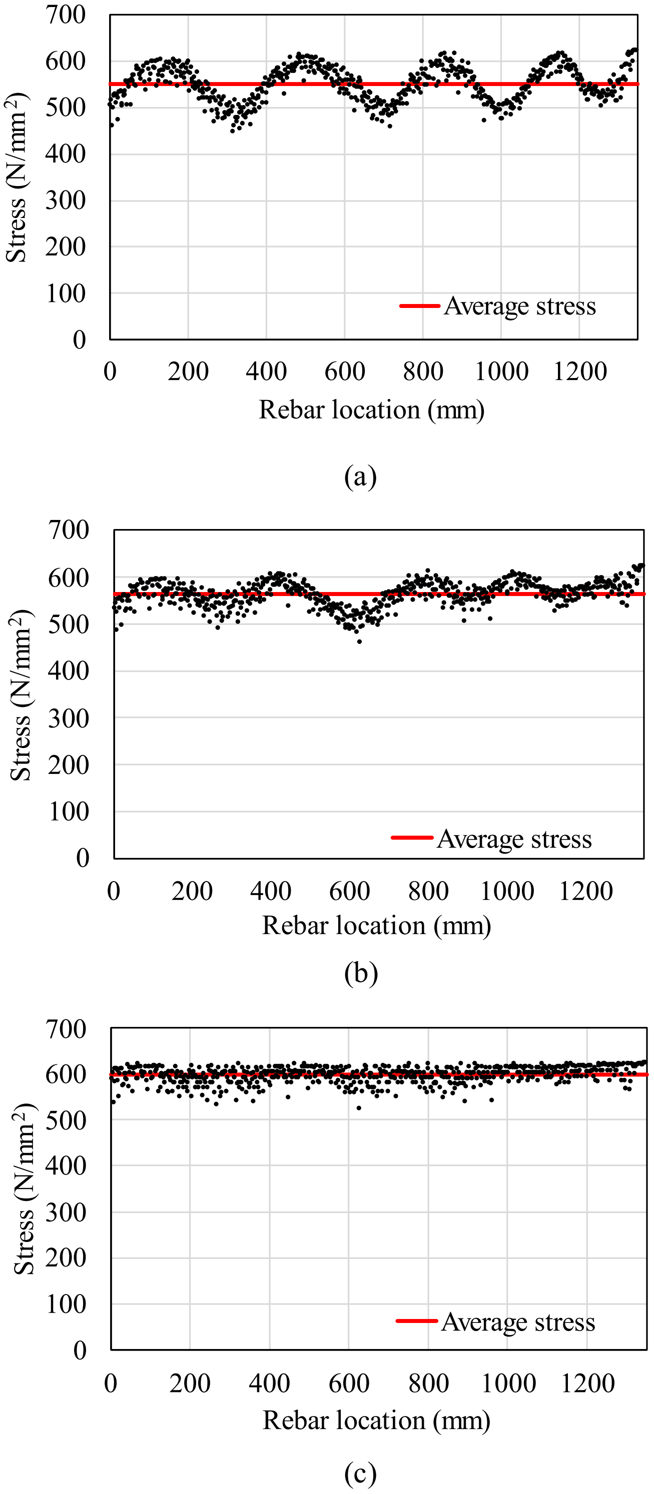

Fig. 16 Stress distribution along the longitudinal axis of rebar elements immediately following the initiation of rebar yielding in RC prisms. (a) Exp-0.1, (b)Exp-0.2, and (c) Exp-0.5

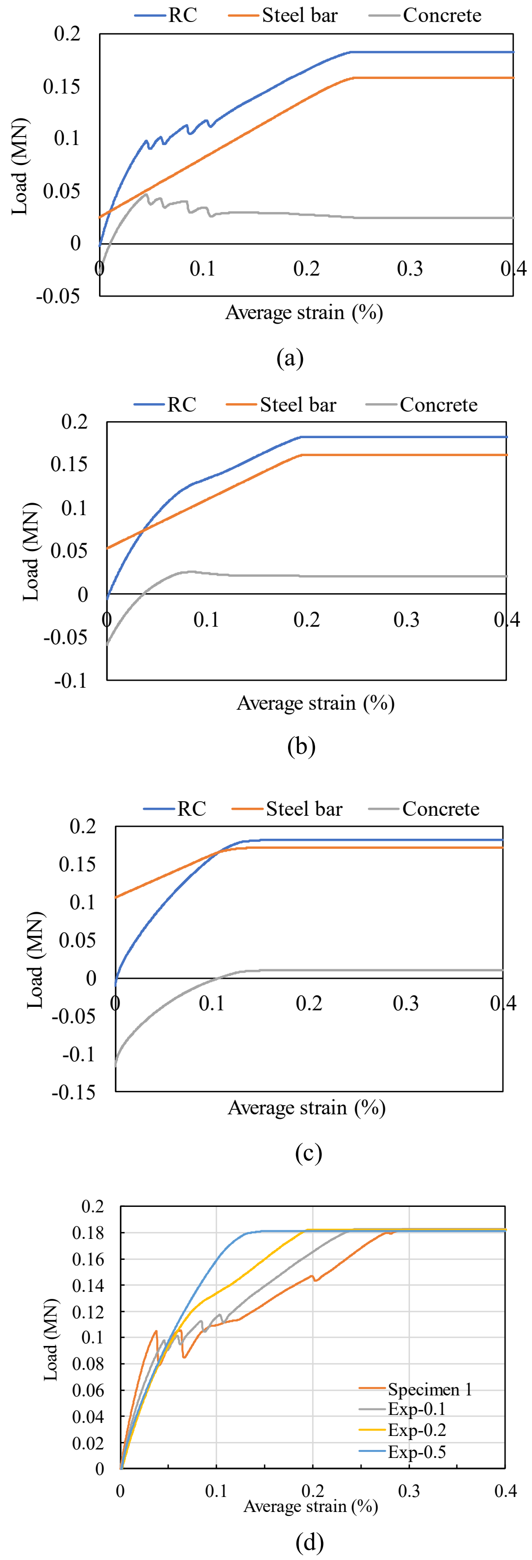

Fig. 17 Relationship between load and average strain in RC prisms (a) Exp-0.1, (b)Exp-0.2, and (c) Exp-0.5, and (d) a comparison including the wet-cured Specimen 1 case.

4. Discussion

When subjected to tensile loading, the concrete in Specimen 1, Specimen 2, Exp-0.1, and Exp-0.2 first attained its tensile strength, then the rebar yielded and the RC prisms each exhibited a plateau in their bearing load. In contrast, the rebar in Exp-0.5 yielded before the concrete attained its tensile strength because the tensile stress in the rebar was already increased owing to RIVE of the aggregate. As a result, the difference between the rebar strain just before loading and at yield was smaller than the increase in concrete strain as it changed from the compression to tensile states. This phenomenon was exacerbated by the reduction in the Young's modulus of the concrete owing to RIVE of the aggregate. Therefore, a quantitative evaluation was performed to evaluate the role of aggregate expansion on the tension stiffening behavior of the RC prisms.

After RIVE of the aggregate, a force balance exists between the concrete and rebar. Thus, the following equations hold under constant-temperature conditions:

$$A_s E_s \varepsilon_{\mathrm{e\_st}} + A_c E_c (\varepsilon_{\mathrm{e\_con}} - \varepsilon_{\mathrm{ex}}) = 0, \tag{2}$$

$$\varepsilon_{\mathrm{e\_st}} = \varepsilon_{\mathrm{e\_con}} = \varepsilon_0, \tag{3}$$

where A_s is the cross-sectional area of the rebar (mm^2), A_c is the cross-sectional area of the concrete (mm^2), E_s is the Young's modulus of the rebar (N/mm^2), E_c is the Young's modulus of the concrete after degradation owing to RIVE of the aggregate (N/mm^2), $\varepsilon_{\mathrm{ex}}$ is the free expansion strain in the concrete owing to RIVE of the aggregate (-), $\varepsilon_{\mathrm{e\_con}}$ is the elastic strain in the concrete, $\varepsilon_{\mathrm{e\_st}}$ is the elastic strain in the rebar, and ε_0 is the average strain in the RC prism (-).

Therefore, the following equation can be derived for the average strain the RC prism:

$$\varepsilon_0 = \frac{A_c E_c}{A_s E_s + A_c E_c} \varepsilon_{\mathrm{ex}}. \tag{4}$$

The axial forces in the concrete (N_c, (N)) and rebar (N_s, (N)) can then be calculated as follows:

$$N_{s,0} = \sigma_{s,0} A_s = \varepsilon_0 E_s A_s, \tag{5}$$
$$N_{c,0} = \sigma_{c,0} A_c = (\varepsilon_0 - \varepsilon_{\mathrm{ex}}) A_c E_c, \tag{6}$$

where σ_s and σ_c are the stresses in the rebar and concrete, respectively, after RIVE of the aggregate (N/mm^2).

A stress–strain relationship for the concrete during the loading process is required that considers the tensile stress region. In the compression and elastic tensile regions, a linear stress–strain relationship can be assumed while accounting for the change in the Young's modulus and tensile strength of the concrete owing to the damage induced by RIVE of the aggregate. The post-peak behavior in the tensile stress region of the concrete can be modeled using the following stress–strain equation according to Okamura and Maekawa (1985):

$$\sigma_c = \begin{cases} E_c(\varepsilon - \varepsilon_{\mathrm{ex}}) & (\varepsilon \le \varepsilon_{tu}) \\ f_t \left(\frac{\varepsilon_{tu} - \varepsilon_{\mathrm{ex}}}{\varepsilon - \varepsilon_{\mathrm{ex}}} \right)^c & (\varepsilon > \varepsilon_{tu}) \end{cases}, \tag{7}$$

where ε is the strain in the concrete (-), f_t is the tensile strength of the radiation-expanded concrete (N/mm^2), $\varepsilon_{tu} = f_t / E_c + \varepsilon_{ex}$ is the strain corresponding to f_t (-), and c is a parameter describing the softening behavior of the concrete (set to 0.4 in this study).

For the rebar, the average strain–stress relationship can be modeled as follows:

$$\sigma_s = \begin{cases} E_s \varepsilon & (\varepsilon \leq \alpha\varepsilon_y) \\ \alpha\varepsilon_y & (\varepsilon > \alpha\varepsilon_y) \end{cases}, \tag{8}$$

where ε is the strain in the rebar (-), ε_y is the rebar tensile yield strain, and α is a factor used to average the stresses in the yielded and non-yielded regions of the rebar. The ratio describing the relative prevalence of these regions is dependent on the damage to and stress distribution in the concrete.

The stress–strain relationship for concrete in which the origin represents the initiation of concrete expansion is shown in Fig. 18(a) using the Young's modulus E_c after RIVE of the aggregate and the resultant stress $\sigma_{c,0}$; similarly, the stress–strain relationship for the reinforcing bar is shown in Fig. 18(b).

The load–strain relationship for the RC prism in which the origin represents the equilibrium strain of concrete expansion owing to RIVE of the aggregate is schematically summarized in Fig. 19 and can be expressed as follows:

$$N = N_s + N_c = \sigma_s A_s + \sigma_c A_c. \tag{9}$$

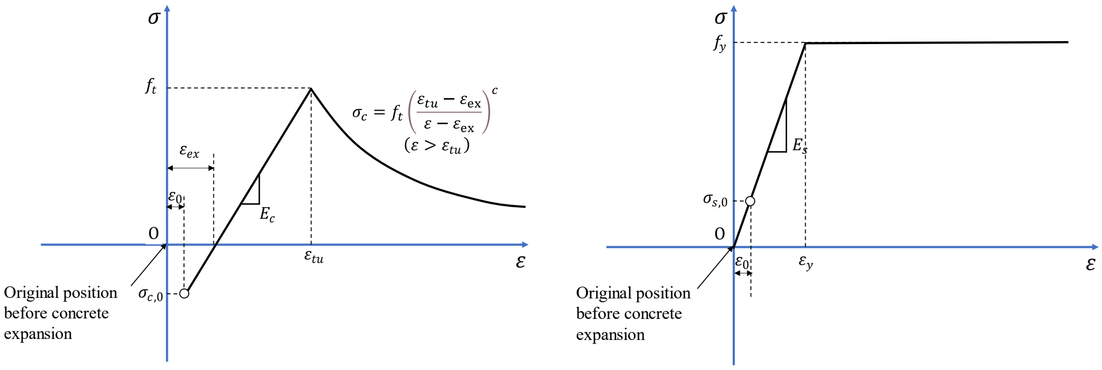

(a) Concrete (b) Steel

Fig. 18 Stress–strain relationships considering the initial stress induced by RIVE of the aggregate.

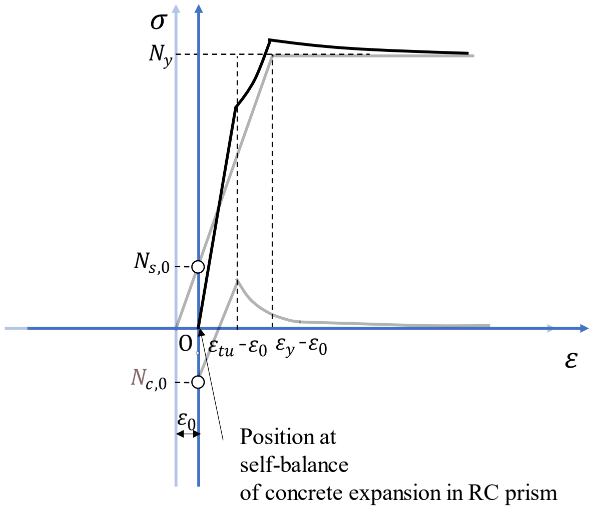

Fig. 19 Load–strain relationship for an RC prism with the origin set at the self-balance state of concrete expansion.

The Young's modulus and tensile strength of the concrete restrained by rebar were estimated using the simplified concept illustrated in Fig. 19 with the results shown in Fig. 20 in terms of the ratio of the tensile strength of each irradiated concrete specimen to the tensile strength of Specimen 1 and the ratio of the Young's modulus of each irradiated concrete specimen to the Young's modulus of Specimen 1. These results are compared with those obtained under the free restraint condition using Eq. (9) from Maruyama et al. (2016) and the relationships shown in Figs. 30 and 31 of Sasano et al. (2020). The comparison indicated that the Young's modulus of concrete under restrained conditions was higher than that under free restraint conditions; this can be explained by the closure of the crack openings in the mortar around the radiation-expanded aggregates owing to the restraint provided by the rebar and the resultant increase in the area over which stress transfer can occur. In contrast, the tensile strength of concrete under restrained conditions was lower than that of concrete under free restraint conditions, likely as a result of anisotropic behavior under unidirectional restraint and the resulting orientation of crack development along the rebar, which enhances the discontinuity of the concrete. To confirm the potential of this simplified model, a comparison with the RBSM results is shown in Fig. 21.

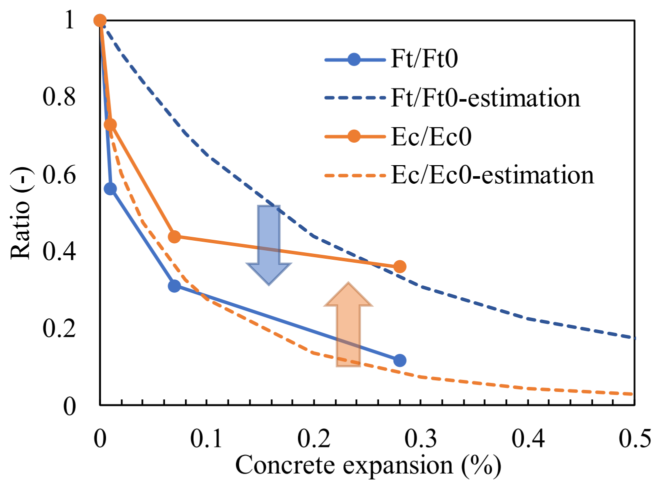

Fig. 20 Comparison of the estimated Young's modulus and tensile strength ratios (value after irradiation/original value) of concrete under rebar restraint with those determined by previous calculations for RC prisms under free restraint.

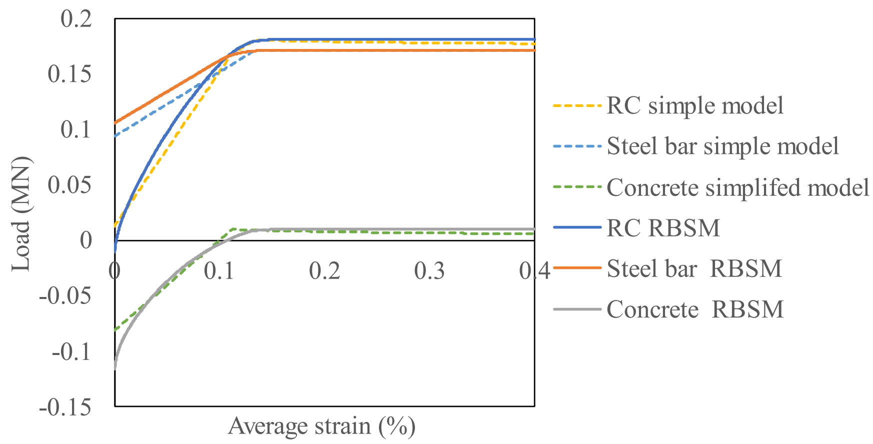

Fig. 21 Comparison of load–strain relationships obtained by RBSM (solid lines) and the simplified model presented in Fig. 19 (dashed lines)

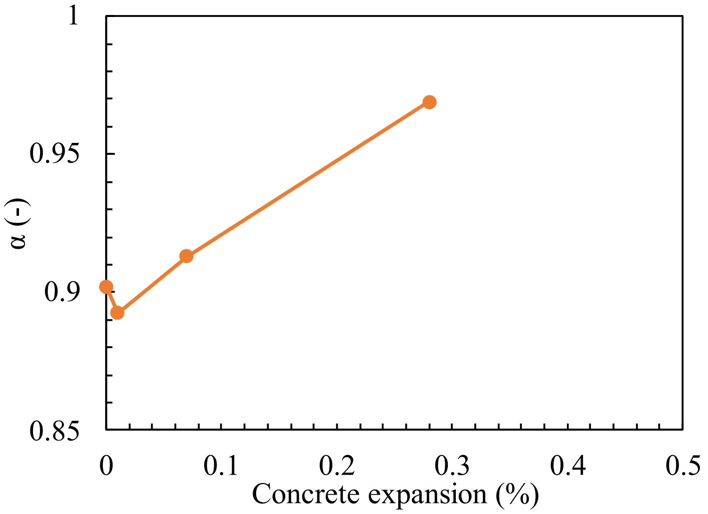

Fig. 22 Value of the factor *α* according to the degree of free concrete expansion, where *α* = 1 indicates that the rebar has completely yielded.

The value of the factor *α* is summarized according to the degree of free concrete expansion in Fig. 22. As more damage to the concrete was induced by RIVE of the aggregate, a longer length of rebar yielded under uniaxial tensile loading (as indicated by a higher value of *α*). As shown in Fig. 15(c), cracks were distributed homogenously owing to RIVE of the aggregate; therefore, the concrete region in which the tensile stress can be borne by the rebar decreased. It can be concluded that the tension stiffening behavior of RC decreases when it is damaged by RIVE of the aggregate. However, it should be noted that, as shown in Fig. 21, the compressive stress induced in the concrete by RIVE of the aggregate was effectively transmitted to the rebar during uniaxial tensile loading, and when the rebar began to yield, the loads borne by the rebar and concrete were accurately reflected by their corresponding material properties. This indicates that the cohesion at the interface between the aggregate and mortar as well as at the crack surfaces in the mortar maintained the integrity of the concrete even after aggregate expansion and subsequent uniaxial tensile loading.

The integrity of the BCS of a nuclear reactor must be ensure by managing the aging of its concrete. Owing to the attenuation of neutrons by the BCS and its relatively large cover depth (~60–100 mm) (Bruck et al., 2019; Kambayashi et al., 2020), the neutron fluence near the rebars after 60 years is 0.3 to 0.15 times the neutron fluence at the internal surface of the BCS (Maruyama et al., 2016; Bruck et al., 2019). Consequently, the neutron fluence range and aggregate volume expansion range discussed in this study include the geometries of most existing reactors. Owing to the difficulty of experimental investigations using limited-scale accelerated irradiation facilities, numerical calculations were conducted to simulate the RIVE phenomenon. The results show that the tension stiffening behavior of RC prisms can be effectively predicted based on existing knowledge of RC structures by considering the changes in the properties of concrete subjected to neutron irradiation under restraint. Special attention should therefore be paid to potential tensile strength reduction owing to inhomogeneous restraint and the increase in the Young's modulus of concrete under restraint (Maruyama et al., 2017).

5. Conclusion

The stresses in RC prisms were numerically investigated using RBSM to understand their tension stiffening behaviors after RIVE of their aggregates. The RBSM method was first validated using wet- and dry-cured (shrinkage) RC prisms subjected to uniaxial loading. The effects of the change in concrete volume on the tension stiffening behavior were shown to be effectively reproduced using RBSM. Then, different degrees of RIVE, previously validated by comparison of neutron-irradiated concrete specimens, were applied to the aggregate elements in the RBSM to evaluate the resulting tension stiffening behavior.

The results indicate that the tension stiffening behavior of RC prisms under restraint can be accurately evaluated according to the property changes induced by neutron irradiation using existing knowledge of RC structures. The Young's modulus of irradiated concrete under uniaxial restraint was shown to be higher than that of irradiated concrete under free restraint, whereas the tensile strength of irradiated concrete under uniaxial restraint was shown to be lower. Consequently, the tension stiffening role of concrete decreased with an increasing degree of RIVE, causing the corresponding damage to increase. These trends should be studied in detail in future research. The compressive stress induced in the concrete by RIVE of the aggregate was shown to be effectively transmitted to the rebar during uniaxial tensile loading of the RC prism, indicating that the integrity of the concrete was maintained even after aggregate expansion.

Acknowledgement

This work was supported by the Japanese Concrete Aging Management Program on Irradiation Effects (JCAMP) funded by the Ministry of Economy, Trade, and Industry, Japan.

Conflicts of Interest

The authors declare no conflict of interest.

CRediT author statement

KD: Writing - original draft, Software

IM: Project administration, Conceptualization, Resources, Methodology, Funding acquisition, Software, Writing - original draft, Writing - review & editing

OK: Funding acquisition, Methodology, Writing - review & editing

SS: Funding acquisition, Writing - review & editing

TO: Methodology, Writing - review & editing

KM: Methodology, Writing - review & editing

KS: Funding acquisition, Project administration, Writing - review & editing

References

Bolander Jr, J. E. and Berton, S., (2004). "Simulation of shrinkage induced cracking in cement composite overlays." *Cement and Concrete Composites*, *26*(7), 861–871.

Bruck, P. M., Esselman, T. C., Elaidi, B. M., Wall, J. J. and Wong, E. L., (2019). "Structural assessment of radiation damage in light water power reactor concrete biological shield walls." *Nuclear Engineering and Design*, *350*(May), 9–20.

Denisov, A., Dubrovskii, V. and Solovyov, V., (2012). *Radiation Resistance of Mineral and Polymer Construction Materials*. ZAO MEI Publishing House.

Elleuch, L. F., Dubois, F. and Rappeneau, J., (1972). "Effects of neutron radiation on special concretes and their components." *American Concrete Institute Special Publication SP-34: Concrete for Nuclear Reactors, 34–51*.

Field, K. G., Remec, I. and Le Pape, Y., (2015). "Radiation effects in concrete for nuclear power plants - Part I: Quantification of radiation exposure and radiation effects." *Nuclear Engineering and Design*, *282*, 126–143.

Friedman, M., Handin, J. and Alani, G., (1972). "Fracture-surface energy of rocks." *International Journal of Rock Mechanics and Mining Sciences*, *9*(6), 757–764.

Hilsdorf, H., Kropp, J. and Koch, H., (1978). "The effects of nuclear radiation on the mechanical properties of concrete." *American Concrete Institute Special Publication SP-55*, 223–251. (被引用数:10Export Date: 16 April 2015)

JSCE, (2002). *Standard Specifications for Concrete Structures—2002, Inspection.*

Kambayashi, D., Sasano, H., Sawada, S., Suzuki, K. and Maruyama, I., (2020). "Numerical analysis of a concrete biological shielding wall under neutron irradiation by 3D RBSM." *Journal of Advanced Concrete Technology*, *18*(10), 618–632.

Kawai, T., (1978). "New discrete models and their application to seismic response analysis of structures." *Nuclear Engineering and Design*, *48*(1), 207–229.

Lin, M., Itoh, M., Maruyama, I., (2015). "Mechanism of change in splitting tensile strength of concrete during heating or drying up to 90 °C." *Journal of Advanced Concrete Technology*, *13*(2), 94–102.

Maruyama, I., Haba, K., Sato, O., Ishikawa, S., Kontani, O. and Takizawa, M., (2016). "A numerical model for concrete strength change under neutron and gamma-ray irradiation." *Journal of Advanced Concrete Technology*, *14*(4), 144–163.

Maruyama, I., Kontani, O., Takizawa, M., Sawada, S., Ishikawa, S., Yasukouchi, J., Sato, O., Etoh, J. and Igari, T., (2017). "Development of soundness assessment procedure for concrete members affected by neutron and gamma-ray irradiation." *Journal of Advanced Concrete Technology*, *15*(9), 440–523.

Maruyama, I., Sasano, H., Nishioka, Y. and Igarashi, G., (2014). "Strength and Young's modulus change in concrete due to long-term drying and heating up to 90 ℃." *Cement and Concrete Research*, *66*, 48–63.

Nakagawa, T., Ohono, Y. and Seo, T., (2008). "Calculation method of shrinkage crack width in reinforced concrete wall using bond-loss length." *Journal of Structural and Construction Engineering (Transactions of AIJ)*, *73*(624), 165–172.

Okamura, H. and Maekawa, K., (1985). "Non-linear finite element analysis of reinforced concrete." *Journal of Japan Society of Civil Engineers*, *1985*(360), 1–10.

Le Pape, Y., (2015). "Structural effects of radiation-induced volumetric expansion on unreinforced concrete biological shields." *Nuclear Engineering and Design*, *295*(December), 534–548.

Le Pape, Y., Sanahuja, J. and Alsaid, M. H., (2020). "Irradiation-induced damage in concrete-forming aggregates: Revisiting literature data through micromechanics." *Materials and Structures 53*(3), 1–35.

Le Pape, Y., Alsaid, M. H. F. and Giorla, A. B., (2018). "Rock-forming minerals radiation-induced volumetric expansion – Revisiting literature data." *Journal of Advanced Concrete Technology*, *16*(5), 191–209.

Primak, W., (1958). "Fast-neutron-induced changes in quartz and vitreous silica." *Physical Review*, *110*(6), 1240–1254.

Sasano, H. and Maruyama, I., (2021). "Mechanism of drying-induced change in the physical properties of concrete: A mesoscale simulation study." *Cement and Concrete Research*, *143*, 106401.

Sasano, H., Maruyama, I., Sawada, S., Ohkubo, T., Murakami, K. and Suzuki, K., (2020). "Meso-Scale modelling of the mechanical properties of concrete affected by radiation-induced aggregate expansion." *Journal of Advanced Concrete Technology*, *18*(10), 648–677.

Shima, H., Chou, L. L. and Okamura, H., (1987). "Micro and macro models for bond in reinforced concrete." *Journal of the Faculty of Engineering*, *39*(2), 133–194.

Wittels, M. and Sherrill, F. A., (1954). "Radiation damage in SiO2 structures." *Physical Review*, *93*(5), 1117–1118. (PR) Retrieved from http://link.aps.org/doi/10.1103/PhysRev.93.1117.2

Yamamoto, Y., Nakamura, H., Kuroda, I. and Furuya, N., (2008). "Analysis of compression failure of concrete by three-dimensional rigid body spring model." *Journal of Japan Society of Civil Engineers*, *64*(4), 612–630.

Yamamoto, Y., Nakamura, H., Kuroda, I. and Furuya, N., (2014). "Crack propagation analysis of reinforced concrete wall under cyclic loading using RBSM." *European Journal of Environmental and Civil Engineering*, *18*(7), 780–792.